

Testing one-zone synchrotron-self-Compton models with spectral energy distributions of Mrk 421

Qianqian Zhu¹, Dahai Yan^{2,3*}, Pengfei Zhang⁴, Qian-Qing Yin^{3,5}, Li Zhang^{1†},
Shuang-Nan Zhang^{3‡}

¹*Department of Astronomy, Key Laboratory of Astroparticle Physics of Yunnan Province, Yunnan University, Kunming 650091, China*

²*Yunnan Observatories, Chinese Academy of Sciences, Kunming 650011, China*

³*Key Laboratory of Particle Astrophysics, Institute of High Energy Physics, Chinese Academy of Sciences, Beijing 100049, China*

⁴*Key Laboratory of Dark Matter and Space Astronomy, Purple Mountain Observatory, Chinese Academy of Sciences, Nanjing 210008, China*

⁵*University of Chinese Academy of Sciences, Beijing 100049, China*

Accepted XXX. Received YYY; in original form ZZZ

ABSTRACT

We test one-zone synchrotron self-Compton (SSC) models with high-quality multi-wavelength spectral energy distribution (SED) data of Mrk 421. We use Markov chain Monte Carlo (MCMC) technique to fit twelve day-scale SEDs of Mrk 421 with one-zone SSC models. Three types of electron energy distribution (EED), a log-parabola (LP) EED, a power-law log-parabola (PLLP) EED and a broken power-law (BPL) EED, are assumed in fits. We find that the one-zone SSC model with the PLLP EED provides successful fits to all the twelve SEDs. However, the one-zone SSC model with the LP and BPL EEDs fail to provide acceptable fits to the highest energy X-ray data or GeV data in several states. We therefore conclude that the one-zone SSC model works well in explaining the SEDs of Mrk 421, and the PLLP EED is preferred over the LP and BPL EEDs for Mrk 421 during the flare in March 2010. We derive magnetic field $B' \sim 0.01$ G, Doppler factor $\delta_D \sim 30\text{--}50$, and the curvature parameter of EED $r \sim 1\text{--}10$ in the model with the PLLP EED. The evolutions of model parameters are explored. The physical implications of our results are discussed.

Key words: radiation mechanisms: non-thermal — galaxies: jets — gamma rays: galaxies

1 INTRODUCTION

Blazars are a class of radio-loud active galactic nuclei (AGN) whose jets point to Earth. Blazar emission extends from MHz radio frequencies to TeV gamma-ray energies. Their spectral energy distributions (SEDs) have two bumps, one peaking at infrared to X-rays, and the other peaking in gamma-ray energies. It is believed that the low-energy bump is the synchrotron emission from high-energy electrons in the jet. The origin of the high-energy bump is still under debate. Leptonic models and hadronic models have been proposed to explain the origin of the high-energy bump. In the leptonic models, the high-energy bump is the inverse-Compton emission from high-energy electrons scattering low-energy photons (e.g., Dermer & Schlickeiser 1993; Sikora et al. 1994). In the hadronic models, the high-energy bump is the synchrotron emissions radiated by high-energy protons

or secondary particles produced in proton-photon interactions (e.g., Mannheim 1993; Mücke & Protheroe 2001; Böttcher et al. 2013).

For high-synchrotron-peaked (HSP) BL Lac objects whose synchrotron peak frequency is greater than 10^{15} Hz (Abdo et al. 2010), a one-zone leptonic synchrotron-self Compton (SSC) model usually provides excellent fits to their SEDs (Abdo et al. 2011a,b; Mankuzhiyil et al. 2011; Zhang et al. 2012; Yan et al. 2014; Zhou et al. 2014). Mrk 421 and Mrk 501 are two of the closest (the redshift $z = 0.031$ and $z = 0.034$ respectively) and brightest TeV HSPs. Many multiwavelength monitoring campaigns for the two typical HSPs have been organized to study their broadband SEDs (e.g., Abdo et al. 2011b; Aleksić et al. 2015; Baloković et al. 2016; Bartoli et al. 2016; Furniss et al. 2015). We recently notice that new extensive broadband data seem to challenge the one-zone SSC model for HSPs. Shukla et al. (2015) constructed the simultaneous SEDs of Mrk 501 from observations during 2011. They claimed that a one-zone SSC model cannot explain the SED of Mrk 501 during 2011 April–May, due to the hard *Fermi*-LAT spectrum.

* E-mail: yandahai@ihep.ac.cn

† E-mail: lizhang@ynu.edu.cn

‡ E-mail: zhangsn@ihep.ac.cn

Furniss et al. (2015) reported the simultaneous broadband observations of Mrk 501 between 2013 April 1 and August 10, including the first *NuSTAR* observations, and modelled the SEDs with a one-zone SSC model. Looking at their modelling results, one can see that the one-zone SSC model cannot reproduce the highest TeV data. Baloković et al. (2016) presented the simultaneous broadband observations of Mrk 421 taken in 2013 January–March, and they modelled these SEDs with a one-zone SSC model. One can see that the SSC model is inconsistent with the GeV–TeV spectrum obtained during 2013 January 15. Mrk 421 was observed at multi-wavelengths for 13 consecutive days during March 2010, and its simultaneous SEDs with unprecedented wavelength coverage from radio frequencies to GeV–TeV energies were built (Aleksić et al. 2015). Aleksić et al. (2015) found that in several states the one-zone SSC model does not match the observed data. In order to match the data, Shukla et al. (2015) and Aleksić et al. (2015) developed a two-zone SSC model for Mrk 501 and Mrk 421.

Although several examples that challenge the one-zone SSC model for Mrk 421 and Mrk 501 are summarized above, one cannot exclude the one-zone SSC model for the two typical HSPs. In our view a key point is missing, i.e., the above studies do not perform searching for parameter space, and therefore the modelling result may not be the best-fit result.

It is important to find convinced evidence for the failures of one-zone SSC model for HSPs. It will motivate us to develop new models, and to find new emission mechanisms, which has a big impact on our understandings of the blazar jet physics.

As mentioned above, Aleksić et al. (2015) reported the day-scale SEDs of Mrk 421 during a flare state in March 2010. These SEDs have unprecedented wavelength coverage. We adopt these high-quality SEDs to test the one-zone SSC model. Given that we do not know the electron energy distribution (EED) in the emission region, we assume three kinds of EED, i.e., a log-parabola (LP) EED, a power-law log-parabola (PLLP) EED and a broken power-law (BPL) EED. The Markov chain Monte Carlo (MCMC) technique is used to search high-dimension parameter space, and to obtain the best-fit result. Throughout this paper, the cosmology with $H_0 = 71 \text{ km s}^{-1} \text{ Mpc}^{-3}$, $\Omega_m = 0.27$, and $\Omega_\Lambda = 0.73$ is adopted.

2 ONE-ZONE SSC MODELS

The one-zone model assumes that non-thermal radiations are produced in a single, homogeneous and spherical region in the jet. The emission region moves relativistically toward us, and consequently the intrinsic radiation is strongly amplified due to the Doppler boosting. Three parameters are needed to characterise the emission region: the comoving magnetic field B' , the Doppler factor δ_D , and the comoving radius of the emission region R'_b which is expressed as $R'_b = c\delta_D t_{\text{var}}/(1+z)$ where t_{var} is the minimum measured variability timescale.

High-energy electrons in the region produce synchrotron photons, and also up-scatter these synchrotron photons to higher energies. The EED in the emission region is uncertain. We adopt three commonly used EEDs. One is the PLLP

EED (e.g., Yan et al. 2013; Zhou et al. 2014; Dermer et al. 2015),

$$\gamma'^2 N'_e(\gamma') \sim \begin{cases} \left(\frac{\gamma'}{\gamma'_c}\right)^{2-s} & \gamma' \leq \gamma'_c \\ \left(\frac{\gamma'}{\gamma'_c}\right)^{2-[s+r \log(\frac{\gamma'}{\gamma'_c})]} & \gamma' > \gamma'_c \end{cases}, \quad (1)$$

where s is the power-law spectral index of the low-energy branch, γ'_c is the cut-off energy of the power-law component, and r is a log-parabola width parameter. The comoving electron energy density is written as $u'_e = \zeta_e u'_B$, where $u'_B = B'^2/(8\pi)$ is the comoving magnetic field energy density, which is used to normalize the EED. Another one is the LP EED (Dermer et al. 2014, 2015; Yan et al. 2015),

$$\gamma'^2 N'_e(\gamma') \sim \left(\frac{\gamma'}{\gamma'_{\text{pk}}}\right)^{-b \log\left(\frac{\gamma'}{\gamma'_{\text{pk}}}\right)}, \quad (2)$$

where b is the spectral curvature parameter, and γ'_{pk} is the peak Lorentz factor in the $\gamma'^2 N'_e(\gamma')$ distribution. The third one is the broken power-law (BPL) EED (Finke et al. 2008)

$$\begin{aligned} \gamma'^2 N'_e(\gamma') \sim & H(\gamma'; \gamma'_{\text{min}}, \gamma'_{\text{max}}) \{ \gamma'^{2-p_1} \exp(-\gamma'/\gamma'_b) \\ & \times H[(p_2 - p_1)\gamma'_b - \gamma'] + [(p_2 - p_1)\gamma'_b]^{p_2-p_1} \gamma'^{2-p_2} \\ & \times \exp(p_1 - p_2) H[\gamma' - (p_2 - p_1)\gamma'_b] \}, \end{aligned} \quad (3)$$

where $H(x; x_1, x_2)$ is the Heaviside function: $H(x; x_1, x_2) = 1$ for $x_1 \leq x \leq x_2$, and $H(x; x_1, x_2) = 0$ everywhere else; as well as $H(x) = 0$ for $x < 0$ and $H(x) = 1$ for $x \geq 0$. γ'_{min} and γ'_{max} are the minimum and maximum energies of electrons, respectively. The spectrum is smoothly connected with indices p_1 and p_2 below and above the break energy γ'_b .

The three EEDs have clear physical origins. An initial single power-law EED can be deformed to become a BPL due to energy losses of electrons (e.g., Yan, Zhang & Zhang 2016). LP function is motivated by the second-order Fermi acceleration (e.g., Becker et al. 2006). Considering a power-law distribution of electrons injected into a turbulent region where second-order processes broaden the distribution, the EED approximates the PLLP function (Dermer et al. 2015).

The SSC radiation spectrum is calculated by the method given by Finke et al. (2008). We adopt the extragalactic infrared–UV background light (EBL) model of Finke et al. (2010) to correct the absorption effect. This EBL model is consistent with other popular EBL models (e.g., Franceschini et al. 2008; Domínguez et al. 2011; Inoue et al. 2013).

The MCMC technique based on the Bayesian statistics is a very powerful fitting tool. It is well suitable to search high-dimension parameter space, and to obtain the uncertainties of the model parameters. Our MCMC code is adapted from the COSMOMC package¹ (Lewis & Bridle 2002) by Liu et al. (2012). Fan et al. (2010) and Yuan et al. (2011) used this code to fit the SEDs of supernova remnants. Yan et al. (2013) applied the MCMC technique to the SEDs of blazars (also see e.g., Zhou et al. 2014; Dermer et al. 2015; Yan et al. 2016).

¹ <http://cosmologist.info/cosmomc/>

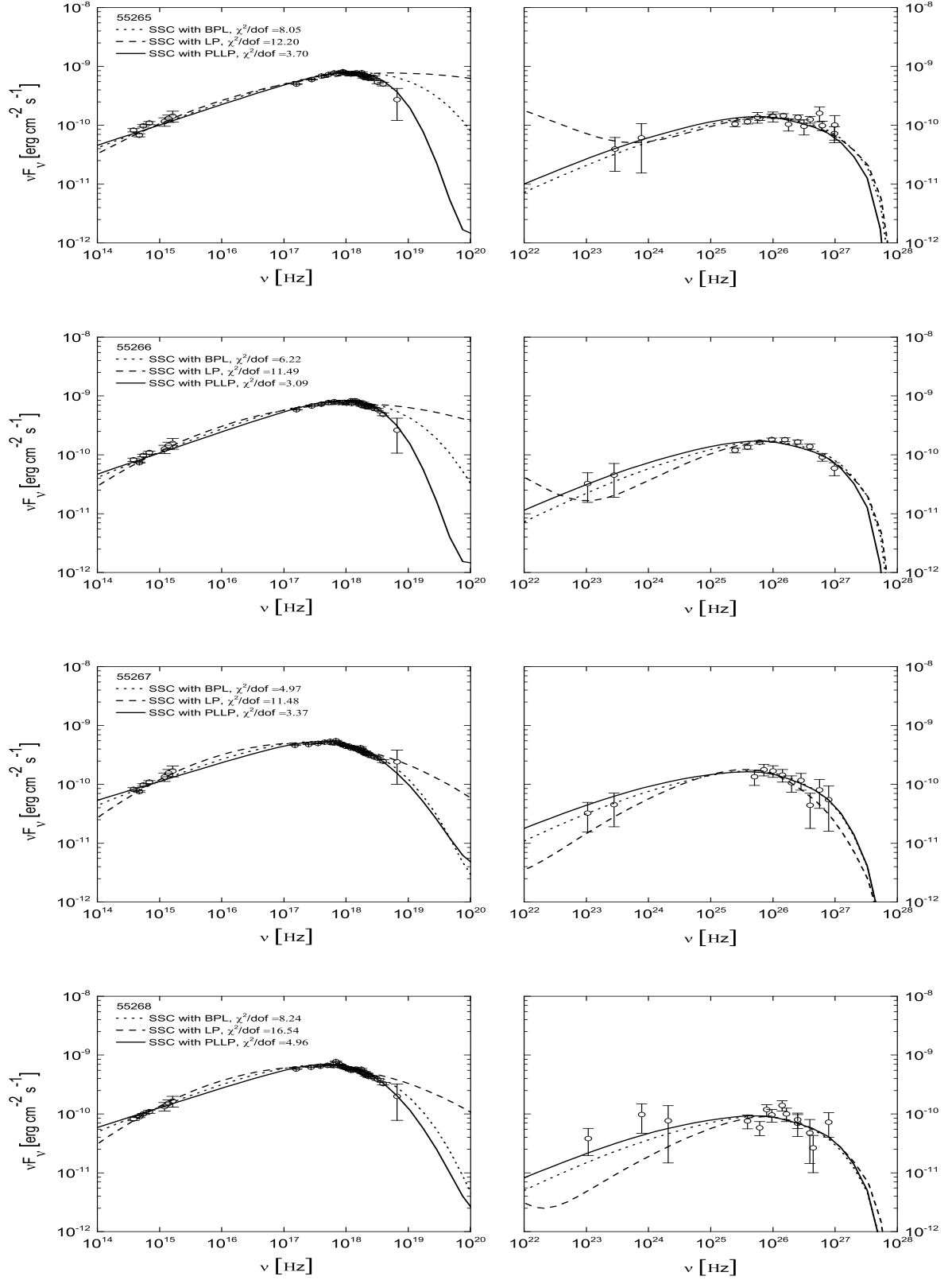


Figure 1. The best fits to the SEDs of Mrk 421 during MJD 55265, 55266, 55267, and 55268 (data from [Aleksić et al. 2015](#)). Solid line: the synchrotron/SSC spectrum with the PLLP EED; Dashed line: the synchrotron/SSC spectrum with the LP EED; Dotted line: the synchrotron/SSC spectrum with the BPL EED. The reduced $\chi^2_{\text{red}} = \chi^2/\text{dof}$ derived in the fits are reported. Left: low-energy bump; right: high-energy bump. Note that though the two bumps in each SED are shown separately the fit is performed simultaneously.

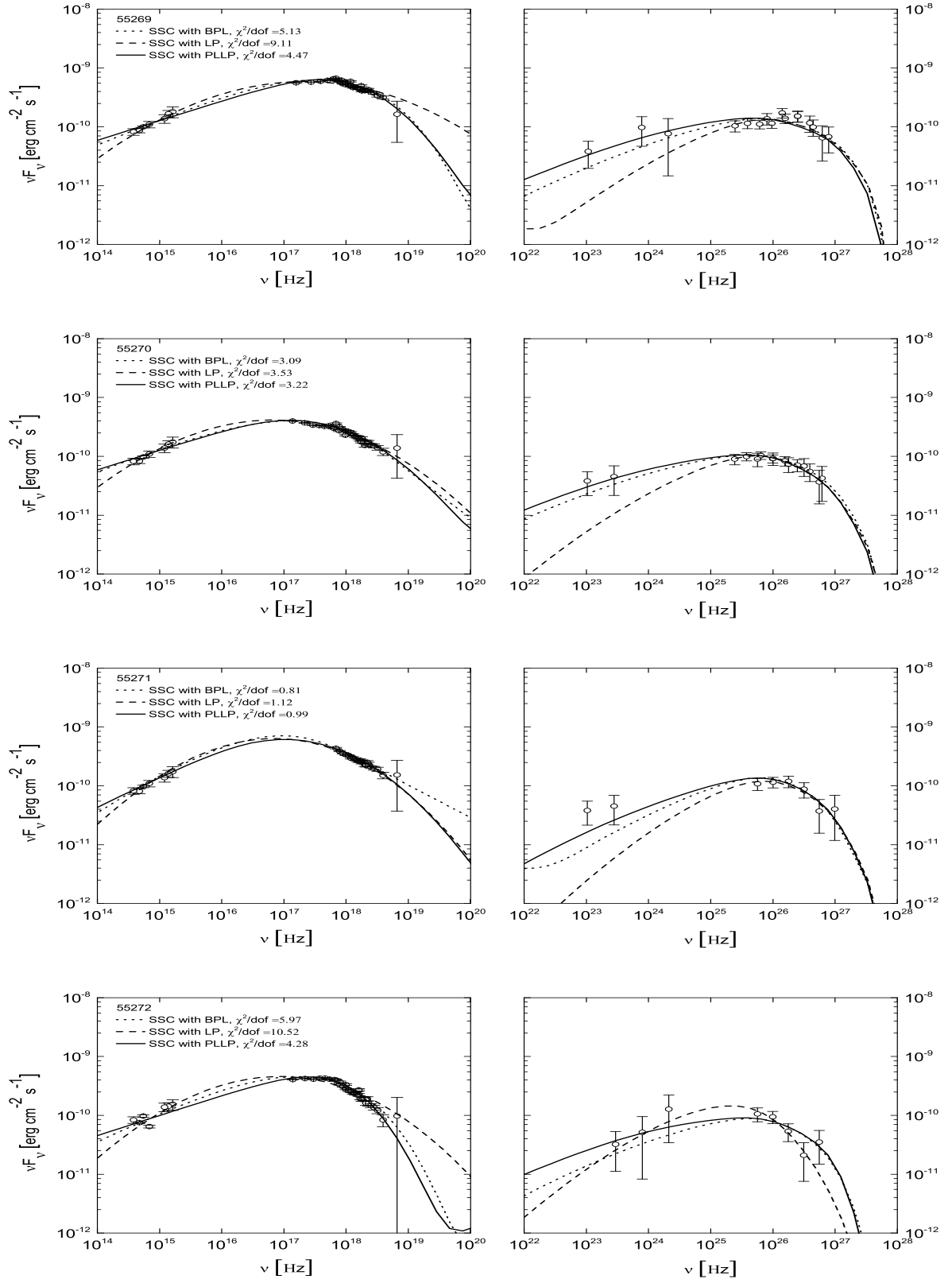


Figure 2. Same as Fig. 1, but for the SEDs during MJD 55269, 55270, 55271, and 55272.

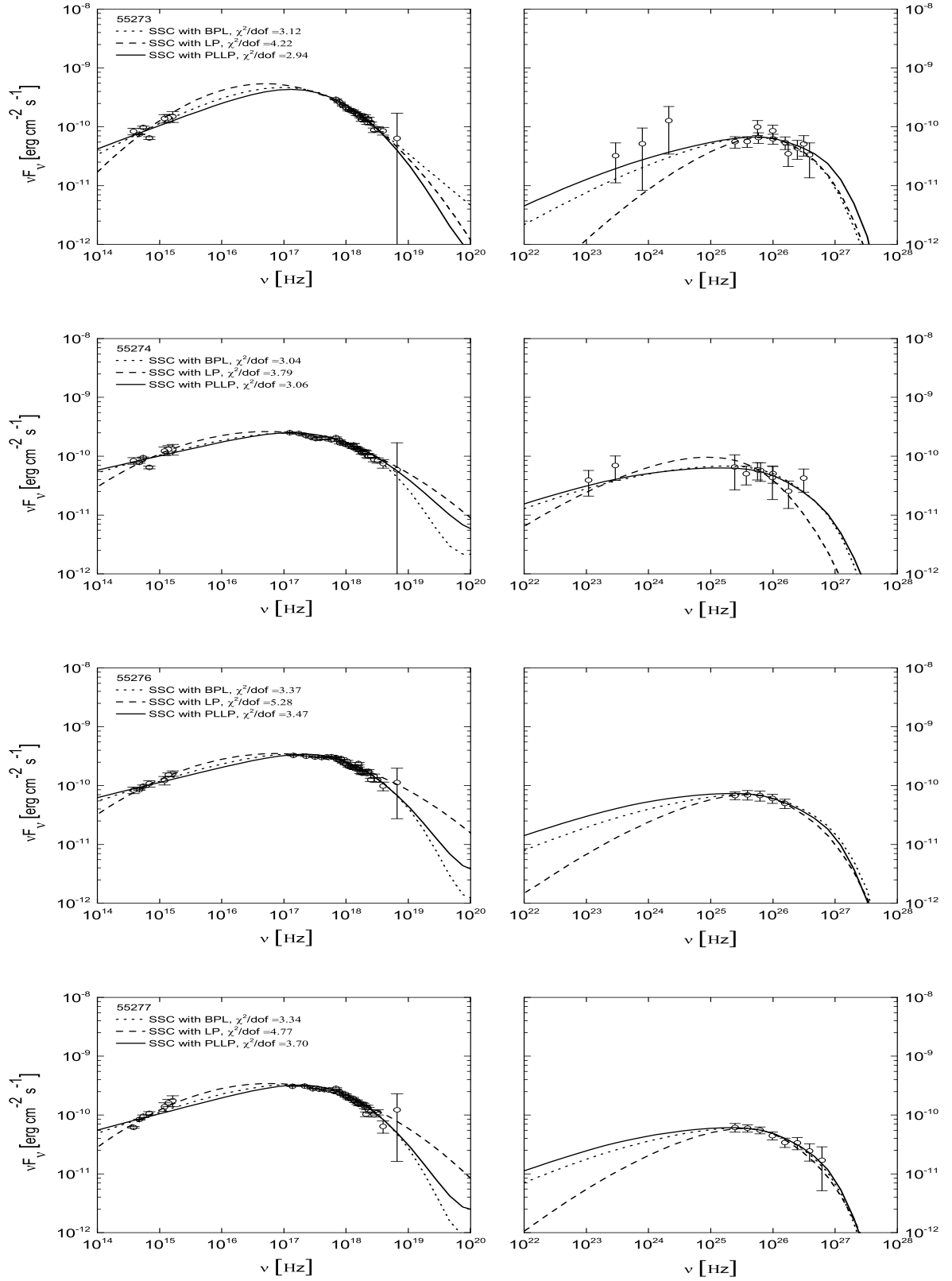


Figure 3. Same as Fig. 1, but for the SEDs during MJD 55273, 55274, 55276, and 55277.

Table 1. Model parameters derived in the one-zone SSC model with the PLLP EED. The mean values and the marginalized 68% confidence intervals (CI) are reported.

MJD	ζ_e	r	B' (0.1 G)	s	t_{var} (10^4 s)	δ_D	γ'_c (10^5)	ν_s^{pk} (10^{17} Hz)
55265 (68% CI)	174 167-200	8.97 8.75-10	0.092 0.085-0.100	2.31 2.30-2.32	8.0 -	32.9 31.8-33.9	11.8 11.4-12.2	15 14-16
55266 (68% CI)	173 169-200	7.54 6.75-10	0.098 0.089-0.11	2.28 2.27-2.29	8.0 -	31.9 30.8-32.8	9.87 9.18-10.53	11 10-12
55267 (68% CI)	145 127-200	2.37 2.18-2.57	0.13 0.01-0.14	2.35 2.34-2.37	8.0 -	28.7 27.7-29.3	4.45 4.12-4.77	2.7 2.4-2.9
55268 (68% CI)	128 100-199	3.19 3.00-3.30	0.12 0.10-0.13	2.33 2.32-2.34	3.0 -	50.0 47.0-52.4	4.41 3.94-4.84	4.0 3.6-4.3
55269 (68% CI)	159 147-200	1.98 1.80-2.17	0.09 0.01-0.10	2.33 2.32-2.34	8.0 -	34.4 33.7-35.4	4.31 3.99-4.62	2.2 1.9-2.4
55270 (68% CI)	98 89-113	1.09 0.98-1.19	0.126 0.001-0.13	2.30 2.26-2.35	8.0 -	31.6 31.1-32.9	1.50 1.21-1.78	0.3 0.2-0.4
55271 (68% CI)	85 63-100	1.22 1.06-1.38	0.099 0.001-0.117	1.99 1.80-2.18	8.0 -	37.7 33.1-42.4	1.27 0.85-1.76	0.2 0.04-0.4
55272 (68% CI)	110 80-200	4.11 3.55-4.68	0.11 0.001-0.12	2.32 2.30-2.33	8.0 -	33.8 31.4-35.8	4.38 3.80-4.93	2.3 2.1-2.6
55273 (68% CI)	53 1-78	2.18 1.84-2.57	0.18 0.10-0.22	2.25 2.16-2.34	8.0 -	30.4 26.9-34.5	2.13 1.90-2.43	0.8 0.6-0.9
55274 (68% CI)	87.8 40-120	1.21 1.04-1.37	0.22 0.13-0.29	2.52 2.49-2.55	8.0 -	26.9 23.1-30.0	1.88 1.55-2.14	0.7 0.4-0.9
55276 (68% CI)	134 112-200	1.89 1.66-2.12	0.11 0.001-0.12	2.48 2.47-2.50	8.0 -	33.4 32.1-35.3	3.23 2.83-3.59	1.4 1.2-1.7
55277 (68% CI)	127 97-200	1.90 1.71-2.10	0.112 0.001-0.113	2.45 2.43-2.46	8.0 -	34.8 33.6-37.5	2.97 2.44-3.41	1.1 0.9-1.3

3 RESULTS

Aleksić et al. (2015) presented 13 day-scale SEDs of Mrk 421. The details on the data and the telescopes can be found in Aleksić et al. (2015). The SED during MJD 55275 has no simultaneous TeV data, therefore we do not include this SED in our study. Using the MCMC technique we fit the rest of 12 SEDs with the one-zone SSC models with three types of EED. The minimum variability timescale for each SED is determined by the observations in Aleksić et al. (2015), which is fixed in the fit.

Figs. 1-3 show the best-fits to the 12 SEDs. It can be easily seen that the one-zone SSC model with the PLLP EED provide excellent fits to all the 12 SEDs; while the one-zone SSC model with the LP and BPL EEDs cannot provide acceptable fits to the highest energy X-ray data in MJD 55265 and MJD 55266. The SSC model with LP EED predicts very hard GeV spectrum in each state and underestimates the GeV emissions. The LP-EED model fails to fit the highest energy X-ray data or the GeV data in most states. To systematically compare the goodness-of-fits with the three EEDs, we plot the reduced $\chi^2_{\text{red}} = \chi^2/\text{dof}$ derived in the fits with the three EEDs in Fig. 4. It can be seen that overall the SSC model with the PLLP EED provide the best fits to the 12 SEDs. In six states, the fits with the

BPL EED are comparable to the fits with the PLLP EED, while in the rest of six states the fits with the BPL EED are significantly worse than the fits with the PLLP EED. It is clear that the PLLP EED is preferred over the LP and BPL EEDs during the flare state in March 2010.

In Table 1 we list the model parameters derived in the one-zone SSC with the PLLP EED. In Appendix A, we give the model parameters derived in the one-zone SSC with the LP and BPL EEDs (Table A1 and Table A2). Here, we focus on analyzing the model parameters derived with the PLLP EED. In Fig. 5, we show the $B' - \gamma'_c$ plot. One can see that the magnetic field B' is ~ 0.01 G during these days. The electron cut-off energy γ'_c varies from 10^5 to 10^6 . It is noted that we derive $\gamma'_c \approx 10^6$ in MJD 55265 and MJD 55266, and a very large $r > 7$. In Fig. 6, one can see that such a large r results in a very sharp high-energy cut-off, and the EED approximates a single power-law. In the two states (MJD 55265 and MJD 55266), we found the peak synchrotron frequency $\nu_s^{\text{pk}} \gtrsim 10^{18}$ Hz. Such a large ν_s^{pk} is rare for HSPs (see the peak synchrotron frequencies reported in Tramacere et al. 2011; Dermer et al. 2015). Fig. 7 shows the $r - \gamma'_c$ plot. It seems that γ'_c is proportional to the curvature r . We adopt a linear function to fit the data, and derive $r = (3.1 \pm 0.3) \text{Log } \gamma'_c - (15 \pm 1)$ with an adjusted $R^2 = 0.7$ and a chance probability $p = 2.5 \times 10^{-4}$.

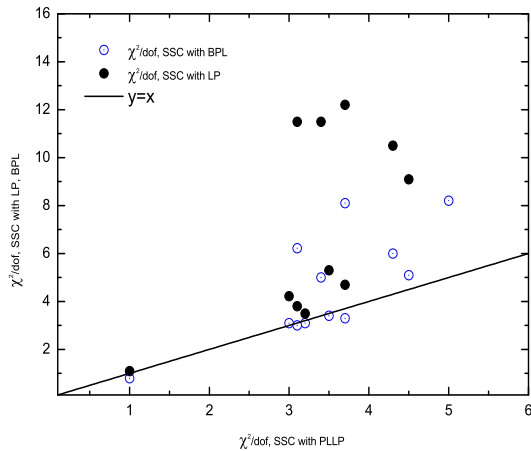


Figure 4. Comparing the reduced χ_{red}^2 derived in the fits to the 12 SEDs with the three EEDs.

In MJD 55268 the TeV emission showed potential intra-night variability (Aleksić et al. 2015), hence we adopt $t_{\text{var}} \approx 8$ hr to fit the SED, and derive $\delta_{\text{D}} \sim 50$. Except this state, we adopt $t_{\text{var}} \approx 22$ hr, and derive $\delta_{\text{D}} \sim 30$ –35.

In Table 1, we also give the values of $\nu_{\text{s}}^{\text{pk}}$ evaluated by the model parameters through the relation $\nu_{\text{s}}^{\text{pk}} \simeq 3.6 \times 10^6 \gamma_c^2 B' \delta_{\text{D}}$ Hz. In Fig. 8, we show the relation of $\nu_{\text{s}}^{\text{pk}}$ and r . We define $\nu_{17} = \nu_{\text{s}}^{\text{pk}}/10^{17}$. We also adopt a linear function to fit the data, and derive $r = (1.6 \pm 0.1) \text{Log } \nu_{17} - (1.9 \pm 0.1)$ with an adjusted $R^2 = 0.8$ and a chance probability $p = 6.1 \times 10^{-5}$. Because of the relation $b_{\text{s}} \simeq r/5^2$ where b_{s} is the curvature of synchrotron bump (Massaro et al. 2004; Tramacere et al. 2011), the trend of $\nu_{\text{s}}^{\text{pk}} - r/b_{\text{s}}$ is different from that reported in previous studies (e.g., Tramacere et al. 2009) where an inverse trend of $\nu_{\text{s}}^{\text{pk}} - b_{\text{s}}$ is presented.

4 DISCUSSION AND CONCLUSIONS

Taking advantage of the MCMC technique (Yan et al. 2013, 2015), we test the one-zone SSC models for Mrk 421 using the high-quality SEDs with unprecedented data coverage reported in Aleksić et al. (2015). According to the fitting results, we conclude that the one-zone SSC model still works well in explaining the broadband SEDs. There is no evidence of a second leptonic/hadronic emission component. Furthermore, our study rules out the LP and BPL EEDs for Mrk 421, and supports the PLLP EED. We determine the magnetic field $B' \sim 0.01$ G and the radius of blob $R'_{\text{b}} \sim [5 - 8] \times 10^{16}$ cm in the PLLP model.

The curvature in electron distribution is related to second-order Fermi acceleration theory (e.g., Becker et al. 2006; Massaro et al. 2006; Stawarz & Petrosian 2008; Tramacere et al. 2011; Yan et al. 2012; Asano et al. 2014).

² Note that the relation $b_{\text{s}} \simeq r/5$ is given by synchrotron emission theory (Massaro et al. 2004), which is robust.

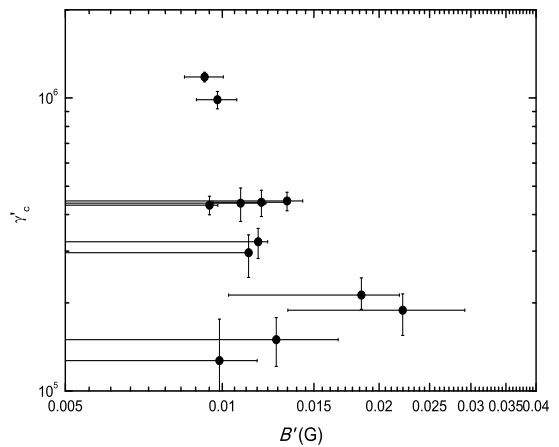


Figure 5. The magnetic field B' versus the cut-off energy of PLLP EED γ_c .

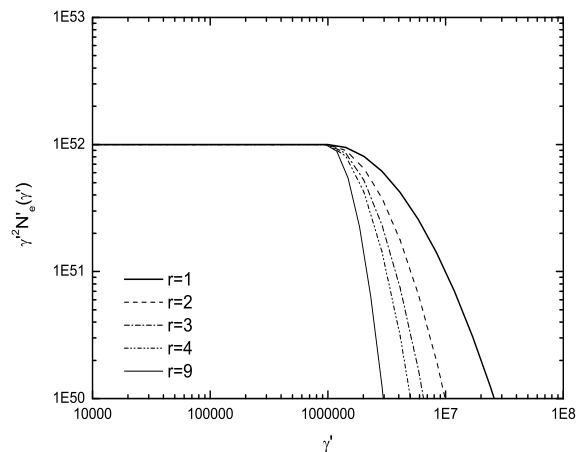


Figure 6. An example to show the impact of the parameter r on the high-energy cut-off shape of PLLP EED.

Second-order processes broaden the injected electron distribution, and introduce a curvature into the energy distribution. Our results that the EED in the jet of Mrk 421 is the PLLP EED implies a scenario combining the first- and second-order Fermi acceleration processes, in which a power-law distribution of particles injected downstream of a shock into a turbulent region where the second-order Fermi acceleration processes broaden the distribution, and then the PLLP EED is formed. The curvature of PLLP EED r in MJD 55265 and MJD 55266 is extremely large, so that the EED is very close to a single power-law distribution. This may be due to the cooling effect (Tramacere et al. 2011).

The evolution of model parameters can reveal the information of physical processes (e.g., Yan et al. 2013, 2016). We find that the cut-off energy γ_c in the PLLP EED in-

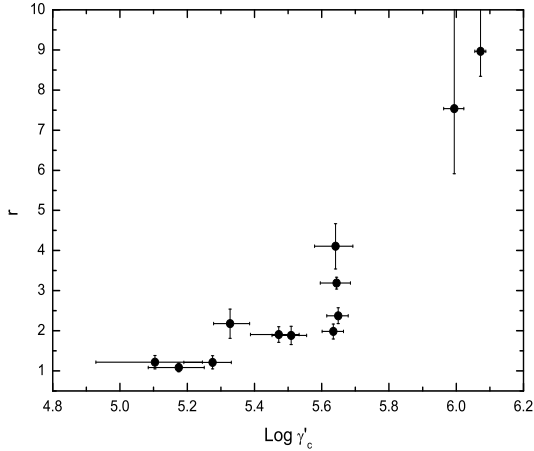


Figure 7. The curvature parameter of PLLP EED r versus the cut-off energy γ'_c .

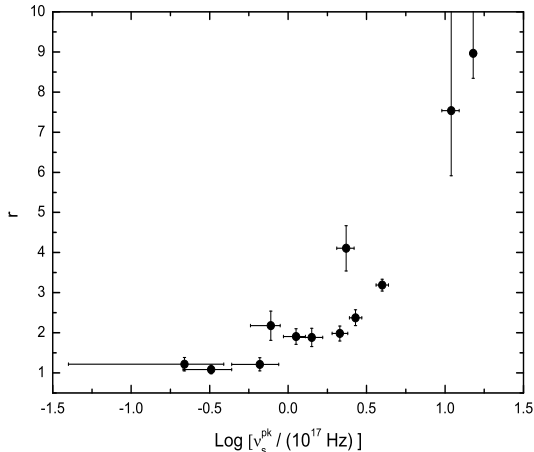


Figure 8. The curvature parameter of PLLP EED r versus the peak synchrotron frequency ν_s^{pk} .

creases with the EED's curvature r . [Tramacere et al. \(2011\)](#) have shown that the curvature r is inversely proportional to the momentum diffusion coefficient when acceleration is dominated over cooling; and r quickly increases once the cooling becomes relevant. The evolution of γ'_c with r (Fig. 5) hints that the radiative cooling of electrons become relevant and the EED approaches the equilibrium between acceleration and cooling. Moreover, the trend of $\nu_s^{\text{pk}} - b_s$ we derived (Fig. 8; using the relation $b_s \simeq r/5$) is different from the inverse correlation found in optical-X-ray data analysis on HSPs (e.g., [Massaro et al. 2006, 2008](#); [Tramacere et al. 2007, 2009](#)). The inverse correlation between ν_s^{pk} and b_s may imply an acceleration-dominated scenario ([Tramacere et al. 2011](#)). From our results, one can see that the evolution of

$\nu_s^{\text{pk}} - b_s$ is the direct representation of the evolution of $\gamma'_c - r$ in the observable space.

[Yan et al. \(2013\)](#) analyzed two SEDs of Mrk 421, respectively, in a quiescent state ([Abdo et al. 2011b](#)) and in a giant TeV flare ([Shukla et al. 2012](#)), and found that the EED in the TeV flare is the PLLP. The 12 SEDs analyzed in this work are obtained in a X-ray and TeV flare state in March 2010 ([Aleksić et al. 2015](#)). It seems that the PLLP EED that involves the first- and second-order Fermi acceleration processes works in the flare state of Mrk 421, and the cooling timescale of electrons with γ'_c may be close to the acceleration timescale. The physical mechanism in quiescent states of Mrk 421 is worth a systematical investigation in a separate study.

As a last remark, we would like to note that an alternative model to explain the SEDs is the leptonic-hadronic model. [Petropoulou et al. \(2016\)](#) explained the 13 SEDs in [Aleksić et al. \(2015\)](#) well with a one-zone leptonic-hadronic model. They derived $B' = 5$ G and $\delta_D \sim 20$, which are different from those derived in the leptonic model. The hadronic model is attractive, since it predicts high-energy neutrinos. To distinguish the leptonic model from the hadronic model is not only important for understanding the jet physics, but also important for resolving the origin of the high-energy cosmic neutrinos, however, it is still very difficult for now.

ACKNOWLEDGMENTS

We thank the anonymous referee for insightful comments that have helped us improve the presentation of the paper. DHY acknowledges funding support by China Postdoctoral Science Foundation under grant Nos. 2015M570152 and 2016T90136, by Key Laboratory of Astroparticle Physics of Yunnan Province (No. 2015DG035) and by the National Natural Science Foundation of China (NSFC) under grant No. 11573026. This work is partially supported by the National Natural Science Foundation of China (NSFC 11433004) and Top Talents Program of Yunnan Province, China. We acknowledge the financial support from the National Natural Science Foundation of China 11573060, the Strategic Priority Research Program, the Emergence of Cosmological Structure of the Chinese Academy of Sciences, Grant No. XDB09000000. SNZ acknowledges partial funding support by 973 Program of China under grant 2014CB845802, by the National Natural Science Foundation of China (NSFC) under grant Nos. 11133002 and 11373036, by the Qianren start-up grant 292012312D1117210, and by the Strategic Priority Research Program “The Emergence of Cosmological Structures” of the Chinese Academy of Sciences (CAS) under grant No. XDB09000000.

REFERENCES

- Abdo A. A., Ackermann M., Agudo I., et al., 2010b, *ApJ*, 716, 30
- Abdo A. A., Ackermann M., Ajello M., et al., 2011a, *ApJ*, 727, 129
- Abdo A. A., Ackermann M., Ajello M., et al., 2011b, *ApJ*, 736, 131
- Aleksić J., Ansoldi S., Antonelli L. A., et al., 2015, *A&A*, 578, 22
- Asano K., Takahara F., Kusunose M., Toma K., Kakuwa J., 2014, *ApJ*, 780, 64

- Baloković M., Paneque, D., Madejski G., et al., 2016, *ApJ*, 819, 156
- Bartoli B., Bernardini P., Bi X. J., et al., 2016, *ApJ*, 222, 6
- Becker P., Le T., Dermer C., 2006, *ApJ*, 647, 539
- Böttcher M., Reimer A., Sweeney K., Prakash A., 2013, *ApJ*, 768, 54
- Dermer C. D., Schlickeiser R., 1993, *ApJ*, 416, 458
- Dermer C. D., Cerruti M., Lott B., Boisson C., Zech A., 2014, *ApJ*, 782, 82
- Dermer C. D., Yan D. H., Zhang L., Finke J., Lott B., 2015, *ApJ*, 809, 174
- Domínguez A., Primack J. R., Rosario D. J., et al., 2011, *MNRAS*, 410, 2556
- Fan Z. H., Liu S. M., Yuan Q., Fletcher L., 2010, *A&A*, 517, L4
- Finke J. D., Dermer C. D., Böttcher M., 2008, *ApJ*, 686, 181
- Finke J. D., Razzaque S., Dermer C. D., 2010, *ApJ*, 712, 238
- Furniss A., Noda K., Boggs S., et al., 2015, *ApJ*, 812, 65
- Franceschini A., Rodighiero G., Vaccari M., 2008, *A&A*, 487, 837
- Inoue Y., Inoue S., Kobayashi M., Makiya R., Niino Y., Totani T., 2013, *ApJ*, 768, 197
- Lewis A., Bridle S., 2002, *PhRvD*, 66, 103511
- Liu J., Yuan Q., Bi X. J., Li H., Zhang X. M., 2012, *PhRvD*, 85, d3507
- Mannheim K., 1993, *A&A*, 269, 67
- Mankuzhiyil N., Ansoldi S., Persic M., Tavecchio F., 2011, *ApJ*, 733, 14
- Massaro E., Perri M., Giommi, P., Nesci R. 2004, *A&A*, 413, 489
- Massaro E., Tramacere A., Perri M., Giommi P., Tosti G., 2006, *A&A*, 448, 861
- Massaro F., Tramacere A., Cavaliere A., Perri M., Giommi P., 2008, *A&A*, 478, 395
- Mücke A., Protheroe R. J., 2001, *Astropart. Phys.*, 15, 121
- Petropoulou M., Coenders S., Dimitrakoudis S., 2016, *Astropart. Phys.*, 80, 115
- Shukla A., Chitnis V. R., Singh B. B., et al., 2015, 798, 2
- Shukla A. et al., 2012, *A&A*, 541, 140
- Sikora M., Begelman M. C., Rees M. J., 1994, *ApJ*, 421, 153
- Stawarz, L., Petrosian, V. 2008, *ApJ*, 681, 1725
- Tramacere A., Massaro F., Cavaliere A., 2007, *A&A*, 466, 521
- Tramacere A., Giommi P., Perri M., Verrecchia F., Tosti G., 2009, *A&A*, 501, 879
- Tramacere A., Massaro E., Taylor A. M., 2011, *ApJ*, 739, 66
- Yan D. H., Zeng H. D., Zhang L., 2012, *MNRAS*, 424, 2173
- Yan D. H., Zhang L., Yuan Q., Fan Z. H., Zeng H. D., 2013, *ApJ*, 765, 122
- Yan D. H., Zeng H. D., Zhang L., 2014, *MNRAS*, 439, 2933
- Yan D. H., Zhang L., Zhang S. N., 2015, *MNRAS*, 454, 1310
- Yan D. H., He J. J., Liao J. Y., Zhang L., Zhang S. N., 2016, *MNRAS*, 456, 2173
- Yan D. H., Zhang L., Zhang S. N., 2016, *MNRAS*, 459, 3175
- Yuan Q., Liu S., Fan Z., Bi X., Fryer C., 2011, *ApJ*, 735, 120
- Zhang J., Liang E. W., Zhang S. N., Bai, J. M., 2012, *ApJ*, 752, 157
- Zhou Y., Yan D. H., Dai B. Z., Zhang L., 2014, *PASJ*, 66, 12

APPENDIX A: MODEL PARAMETERS DERIVED IN THE FITS WITH THE LP AND BPL EEDS

This paper has been typeset from a $\text{\TeX}/\text{\LaTeX}$ file prepared by the author.

Table A1. Model parameters derived in the one-zone SSC model with the LP EED. The mean values and the marginalized 68% confidence intervals (CI) are reported.

	ζ_e	b	B' (0.1G)	t_{var} (10^4 s)	δ_D	γ'_{pk} (10^4)
55265 (68% CI)	44.0 42.8-50.0	0.26 0.25-0.27	0.108 0.096-0.12	8.00 -	33.8 32.7-34.8	2.88 2.58-3.16
55266 (68% CI)	44.8 43.8-50.0	0.37 0.36-0.37	0.102 0.096-0.108	8.00 -	34.2 33.3-35.0	4.91 4.68-5.15
55267 (68% CI)	19.4 0.01-50.0	0.56 0.55-0.57	0.252 0.072-0.396	8.00 -	27.2 21.3-33.2	4.30 3.45-5.17
55268 (68% CI)	26.8 19.17-50.0	0.52 0.51-0.53	0.132 0.06-0.18	3.00 -	55.8 47.5-63.9	4.09 3.47-4.68
55269 (68% CI)	39.4 36.5-50.0	0.56 0.55-0.57	0.084 0.072-0.096	8.00 -	39.8 37.6-41.9	5.95 5.56-6.34
55270 (68% CI)	30.1 24.2-50.0	0.71 0.70-0.73	0.096 0.06-0.12	8.00 -	39.4 35.0-43.6	4.98 4.41-5.52
55271 (68% CI)	24.6 17-50.0	0.96 0.92-1.00	0.096 0.036-0.132	8.00 -	43.1 36.1-49.9	7.62 6.43-8.82
55272 (68% CI)	3.6 0.01-2.9	0.83 0.81-0.84	0.816 0.288-1.356	8.00 -	20.5 14.3-26.5	3.85 2.93-4.70
55273 (68% CI)	12.8 0.01-14.1	1.16 1.12-1.20	0.108 0.06-0.168	8.00 -	44.4 36.9-52.1	7.42 6.12-8.74
55274 (68% CI)	16.8 0.01-50.0	0.61 0.59-0.62	0.42 0.001-0.3	8.00 -	31 18.3-42.6	2.67 1.67-3.59
55276 (68% CI)	22.2 0.01-50.0	0.61 0.60-0.62	0.12 0.001-0.132	8.00 -	38.5 31.3-45.6	3.64 2.96-4.30
55277 (68% CI)	10.3 0.01-11.2	0.69 0.68-0.70	0.18 0.084-0.252	8.00 -	35.2 28.9-41.7	3.57 2.97-4.19

Table A2. Model parameters derived in the one-zone SSC model with the BPL EED. The mean values and the marginalized 68% confidence intervals (CI) are reported.

MJD	ζ_e	p_2	B' (0.1 G)	p_1	t_{var} (10^4 s)	δ_{D}	γ'_c (10^5)
55265 (68% CI)	171 165-200	7.47 6.63-10	0.080 0.073-0.087	2.19 2.18-2.21	8.0 -	34.6 33.5-35.7	18.39 17.53-19.22
55266 (68% CI)	165 157-200	7.48 6.62-10	0.083 0.010-0.084	2.12 2.11-2.13	8.0 -	33.9 32.6-35.2	12.98 12.42-13.53
55267 (68% CI)	84 54-94	7.77 6.52-9.14	0.165 0.001-0.201	2.13 2.12-2.14	8.0 -	27.3 16.0-28.7	6.29 5.57-7.24
55268 (68% CI)	117 93-200	7.98 7.31-10	0.093 0.075-0.101	2.11 2.10-2.12	3.0 -	55.0 52.6-58.1	6.37 5.00-6.74
55269 (68% CI)	159 147-200	7.39 6.47-10	0.071 0.001-0.074	2.12 2.10-2.13	8.0 -	37.9 37.1-38.9	7.91 7.47-8.31
55270 (68% CI)	158 143-200	6.42 5.12-10	0.077 0.001-0.082	2.19 2.17-2.21	8.0 -	37.1 36.1-37.7	5.31 5.03-5.59
55271 (68% CI)	61 1-70	4.16 4.07-4.24	0.107 0.001-0.126	1.69 1.55-1.81	8.0 -	37.9 32.9-40.8	2.52 2.19-2.78
55272 (68% CI)	67 36-72	7.45 7.02-7.90	0.110 0.001-0.139	1.97 1.96-1.99	8.0 -	35.5 30.5-38.5	4.20 3.72-4.48
55273 (68% CI)	120 102-200	5.68 4.78-5.87	0.050 0.042-0.050	1.87 1.72-2.00	8.0 -	45.5 43.0-45.0	3.76 3.17-4.25
55274 (68% CI)	96 63-200	7.04 6.22-10	0.153 0.103-0.170	2.35 2.34-2.37	8.0 -	30.5 27.8-33.5	5.27 4.84-5.79
55276 (68% CI)	112 73-200	8.26 7.72-10	0.102 0.001-0.116	2.27 2.25-2.28	8.0 -	36.0 33.3-39.3	5.76 5.33-6.31
55277 (68% CI)	61 28-73	8.66 8.32-9.11	0.140 0.001-0.190	2.21 2.20-2.22	8.0 -	33.5 28.7-36.4	4.46 3.91-4.83